Electron Density Response to Phonon Dynamics in MgB₂: An Indicator of Superconducting Properties

Jose A. Alarco, Peter C. Talbot, Ian D. R. Mackinnon

Institute for Future Environments and Science and Engineering Faculty, Queensland University of Technology (QUT), Brisbane, Australia
Email: jose.alarco@qut.edu.au, p.talbot@qut.edu.au, ian.mackinnon@qut.edu.au

Abstract

Electron density differences resulting from atom displacement patterns aligned with phonon modes in MgB₂ have been calculated using density functional theory (DFT). The extent of phonon anomalies, identified as indicators of the superconducting transition temperature, T_c, under a range of conditions in AlB₂-type structures, reduce as boron atoms are displaced from their equilibrium positions along E_{2g} mode directions. The Fermi energy for displacements along the directions of the E_{2g} phonon mode accounts for changes in the covalent B−B bond electronic charge density. We applied differential atom displacements to show that the shifted σ band structure associated with the light effective mass became tangential to the Fermi level and that the Fermi surface undergoes a topological transition at a critical relative displacement of ~0.6% of the boron atoms from equilibrium. The difference in Fermi energies at this critical displacement and at the equilibrium position correspond to the superconducting energy gap. The net volume between tubular σ surfaces in reciprocal space correlated with the depth of the phonon anomaly and, by inference, it is a key to an understanding of superconductivity. This *ab initio* approach offers a phenomenological understanding of the factors that determine T_c based on knowledge of the crystal structure.

Keywords

Electron Density, MgB₂, Phonon Dispersion, Kohn Anomaly, Phonon Dynamics, Superconducting Transition Temperature, Superconductivity Mechanism

1. Introduction

Density Functional Theory (DFT) offers an effective alternative to solution of a

many-body Schrodinger wave equation for multi-atom structures to determine the ground state electronic properties of a crystalline material [1]. For many materials including superconductors, DFT provides facile resolution of fine-scale structural variations (*i.e.* picometer) because electron density is the key variable in real, three-dimensional coordinate space for a particular crystallography [1]. This fundamental attribute of DFT arises because charge distribution calculations are an explicit feature of these methods [2]. It follows then, that detailed analysis of calculated charge distributions could provide insight into the underlying mechanisms of superconductivity and other electron dependent phenomena. We evaluate charge distributions in the boron-boron (B−B) plane of a conventional superconductor, MgB_2, that complement earlier work on phonon distributions in the type structure. There are many theoretical and experimental studies on MgB_2 extant in the literature. This abundance of information combined with a simple structure containing two atom types provides an excellent reference for detailed DFT modelling of electron distributions in a conventional BCS superconductor.

The superconducting transition temperature, T_c, not only determines the practical applicability of a superconducting material, but it also helps identify mechanisms from which superconductivity emerges [3]. Current approaches to determine the T_c of a material from knowledge of its crystal structure still rely on adjustment of Coulomb pseudo-potentials and effective electron phonon coupling constants; thus, significant *ab initio* value and prediction capacity are lost. In light of excellent correlations found between temperatures derived from anomalies in phonon dispersions and T_c for AlB_2 type compounds [4] [5], under a wide range of external conditions and without any corrections or adjusting parameters [6] [7], this work explores electron density responses to the phonon dynamics. This *ab initio* approach provides a basis for design of new materials with *a priori* predictable superconducting transition temperatures.

A valuable contribution to superconductivity models is the use of DFT to calculate the deformation potentials [8] of MgB_2, a superconductor at 39 K [9]. This approach determines the amount of energy that breaks the degeneracy of σ electronic bands per unit length of B−B inter-bond distances. These distances are modified according to specific vibration patterns and then frozen in a model calculation [2]. Using this approach, An and Pickett [2] observe that the displacement patterns of B_{1g}, A_{2u}, and E_{1u} modes produce no visible effect in the electronic bands of MgB_2. They estimate that the deformation potentials of these modes are at least a factor of 25 smaller than those for displacement patterns associated with the E_{2g} mode [2]. This approach clearly identifies the E_{2g} vibration mode as a key factor in the superconducting mechanism for MgB_2 as emphasised by many researchers [10] [11] [12]. However, the variation of these modes, or of the total population of these modes, with temperature and the interplay between inter-bond distances with temperature are less evident even though these features may be directly relevant to superconductivity mechanisms. In this work,

we explore these variations of modes with inter-bond distance which we show corresponds to effects of temperature.

Recently, deformation potentials have been used in McMillan equations to explain the effects of structural parameters on the T_c of MgB_2 and substituted forms [7] [8]. The McMillan equation determines reasonably well the T_c of known superconductors based on normal state parameters [8] [10] [13]. This fact offers hope that standard DFT may provide all the necessary characteristics of a superconducting material based only on knowledge of the crystal structure [14]. However, the temperature dependencies of T_c estimates using McMillan equations are often not identified in preference to comparisons of the electron density of states for different related structures [7] [8]. For example, recent attempts to identify thermal effects on superconductivity from lattice vibrations invoke zero point lattice fluctuations [15] without consideration of increased amplitude of vibration for temperatures above 0 K.

We now extend these concepts and, in taking a lead from the early work of An and Pickett [2], use DFT calculations to examine the deformation of specific atomic bonds or their charge distribution relevant to particular vibration modes within a structure. We also make an explicit correlation of the increased amplitude of vibration expected as a function of temperature for different phonon modes. In this work, we show that such an approach using *ab initio* DFT methods is an effective way to visualise the transition to superconductivity in MgB_2. In addition, we use this approach to re-examine the effects of displaced atom positions that align with key phonon vibration modes on the electronic properties of MgB_2. We utilize this technique to identify specific response(s) of electron density to these atom displacements and relate these effects to changes in the Fermi energy and Fermi surface of MgB_2. These changes, explicitly determined using DFT calculations, explain variations of the depth of phonon dispersion (PD) anomalies with strong correlation to T_c [5] [6], directly influence superconductivity and establish a direct connection to variations in temperature. While these correlations are exemplified for MgB_2 in this article, we submit that this phenomenological approach is applicable across a broad range of compounds.

2. Computational Methods

DFT calculations are undertaken using the CASTEP module of Materials Studio 8.0, using the linear response method from this software suite [16] [17]. The linear response within the Local Density Approximation (LDA) and Generalized Gradient Approximation (GGA) with norm-conserving pseudo-potentials, a plane-wave basis set and a dense k-grid provide the most consistent model outcomes for the MgB_2 structure [4] [5] [6]. Calculations are undertaken with a High-Performance Computing (HPC) facility, using numbers of cores which are multiples of the k grids defined in the reciprocal $a^{\star}$ and $b^{\star}$ directions of the MgB_2 Brillouin zone. The number of HPC cores is typically between 60 and 80.

Unless specified, calculations have been customized to spin-unpolarized metal, cut-off energy 990 eV, a non-relativistic treatment and convergence criteria as follows: energy at 5×10^{-6} eV per atom; maximum force at 0.01 eV Å^{-1}; maximum stress at 0.02 GPa and maximum atom displacement at 5×10^{-4} Å.

For unit cell calculations on MgB_2 with P6/mmm symmetry, lattice parameters $a = b = 3.085$ A and $c = 3.523$ A are used as input values [9] [18] [19]. For electronic band structure calculations, the computation time is significantly shorter than that required for PD calculations [5]. Therefore, higher resolution grids (*i.e.* for k-grid separation $\Delta k < 0.02$ A^{-1}) are utilized for band structure calculations. We also define relative atom displacement values, D_x, in terms of relative unit cell coordinates for the B−B plane. Thus, a value for $D_x = 0.008$ defines a movement, or displacement of the boron atoms, along a real space direction relative to the *a* lattice parameter of 0.8% relative where the cell parameter is 1.0. Using the unit cell dimensions for MgB_2, this example represents a displacement of 2.468 pm. A positive or negative sign for the D_x value designates an extension or compression of the atom-atom displacement, respectively. This atom displacement is annotated with respect to the B−B plane due to its significant contribution to superconductivity in MgB_2 [2] [11] [13].

Materials Studio 8.0 allows for the determination of electron density differences and electron localization functions by selecting appropriate options in the set-up for each calculation [17]. Materials Studio provides the option of generating the electron density difference in two different ways: 1) to calculate electron density differences with respect to a linear combination of the atomic densities or 2) to calculate the electron density differences with respect to a linear combination of the densities of sets of atoms contained in the model. Alternatively, the program provides for both approaches to be selected simultaneously. For this work, electron density differences are calculated with respect to a linear combination of the atomic densities.

The electron localization function (ELF) provides a useful qualitative description of chemical bonding. This function, retrievable from Materials Studio 8.0 through set-up conditions, follows the approach introduced by Becke and Edgecombe [20] and the revised interpretation in more recent literature [21]. The outputs from electron density difference and electron localization function calculations are very sensitive to choice of the iso-value for the corresponding iso-surfaces. Within a comparison series, iso-values are selected in order to enhance the contrast of properties but are maintained at constant value within a series of computations. This approach highlights the influence of the displacement parameter and changes made to this parameter in a computational series.

Electron density differences are determined for symmetric arrangements of atoms and for corresponding modified positions that are displaced along orientations aligned with particular phonon modes. This computational approach is similar to calculations used by An and Pickett [2] to determine deformation potentials. Deformation potentials in conjunction with McMillan's formulation

[22], are shown to successfully estimate T_c for MgB_2 [8]. This approach is visually demonstrated on two web sites [23] [24] which display the dynamic behaviour of σ electronic bands that are strongly linked to E_{2g} phonon modes in MgB_2.

For the initial structural model, geometry optimization is undertaken as reported previously [4] [5]. However, for subsequent calculations in which an atom displacement position is assumed, further geometry optimization is not undertaken. In this way, a frozen picture of the electron distribution at an intermediate position of the particular phonon mode is created. We have evaluated displacement patterns corresponding to the A_{2u}, E_{1u} and both E_{2g} modes, as described by Kunc *et al.* [10]. For the E_{2g} modes, these displacement patterns predominantly involve boron atoms in the *a-b* plane.

With displaced atom positions frozen in place, electronic band structures are calculated using the selected configuration with appropriate consideration of structural symmetries invoked by the displaced atom positions. By constraining these atom positions to a new symmetry condition, the computation is simplified and the calculation time is reduced. We have demonstrated in earlier work [5] [6] [7] that comparison of models using the LDA and GGA functionals provides an excellent measure of internal consistency for AlB_2-type structures and a source of error estimates for a generic model.

In order to calculate the phonon dispersions (PD's) for displaced positions of boron atoms, geometry optimization is required, and may be limited to atom projections without changing lattice parameters. To prevent geometry optimization from relocating displaced atoms to their equilibrium positions, a primitive symmetry and very high force convergence tolerances are used. For the MgB_2 structure, force tolerances of 0.35 eV/Å and 0.5 eV/Å are required for bond distance changes up to ±0.006 (= ±0.6%) and for ±0.008 (= ±0.8%) in terms of relative coordinates. Thus, large restoring forces are maintained and accordingly, computational models achieve convergence for PD calculations. Because these PD calculations are computationally intense (using 196 q-points), we have limited this type of study to one E_{2g} PD mode and the corresponding σ band Fermi surface using the LDA functional. Outcomes from this calculation are shown in Section 3.3 for selected displaced atom positions with reduced symmetry approximating the **G−A**, **G−K** and **G−M** directions.

3. Modelling Results

We present modelling outcomes in the following sections that analyse the impact of atom displacement on phonon modes and on band structure. Section 3.1 identifies the phonon modes that produce electron density differences as a result of an induced "frozen" displacement pattern. The modes that induce electron density differences are described in detail in Section 3.2 through effects on the electronic bands with increased atom displacement from an equilibrium position. We briefly describe the influence of these atom deformations on Fermi energies and their surfaces. Finally, Section 3.3 confirms that at an appropriate

displacement from equilibrium, the phonon anomalies collapse with clear implications for the Fermi surfaces and, by inference, for superconductivity of MgB_2.

3.1. Electron Density

As noted, the choice of iso-value greatly influences the visual representation of electron density differences and the electron localization function. Furthermore, to illustrate the influence of atom displacement, we show in Figure 1 the difference in electron density (in blue) for the symmetric MgB_2 structure and for two situations with perpendicular in-plane displacements of boron atoms. These in-plane displacement directions correspond to two different E_{2g} modes in the MgB_2 structure, with an exaggerated relative displacement of +0.05 (in relative coordinates) using the same iso-value of 0.15. This relative displacement value may be extreme compared to what is physically reasonable. However, the displacement demonstrates that substantial changes to the electron density occur within the *a-b* plane of the MgB_2 structure when boron atoms are shifted along the dominant optical phonon mode direction.

For each calculation represented in Figure 1, the iso-value is kept constant in order to avoid introducing secondary effects on these results. Figure 1 demonstrates that electron density migrates from regions with longer B–B distances to regions with shorter B–B distances. This outcome is not unexpected because an increase in B–B repulsion requires a corresponding response in electronic bond charge population to reduce the overall energy. However, the sustained localization of the electron density differences along the highly covalent B–B bonds is informative. Similar visualizations of electron density differences can be obtained for smaller atom displacements with appropriate adjustment of the iso-value.

(a) (b) (c)
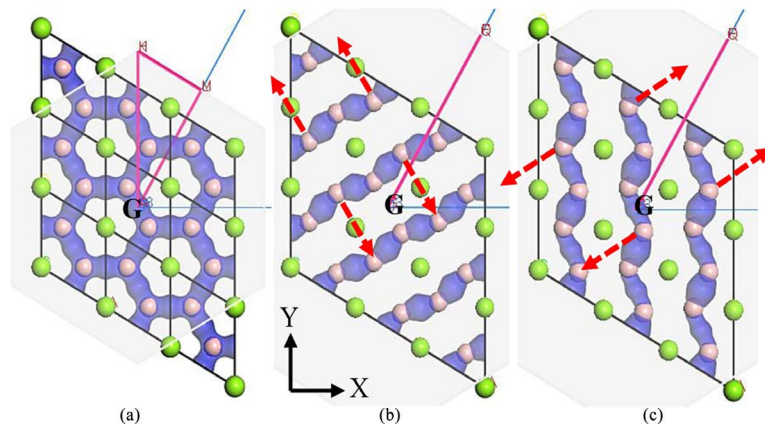
Figure 1. Calculated representations of electron density differences (in blue) for MgB_2 viewed along a direction equivalent to the *c*-axis: (a) the symmetric structure without atom displacements; (b) and (c), with two perpendicular in-plane displacements of boron atoms (red dashed arrows show direction) corresponding to the E_{2g} modes. Mg atoms are in green, boron atoms are pink. Note the substantial modulation of electron density aligned with planar boron atoms for displacements along E_{2g} directions.

For comparison, we also show the effects on electron density with atom displacements along the A_{2u} vibration mode in **Figure 2**. In **Figure 2**, the relative displacement of boron atoms is the same as used for calculations shown in **Figure 1** (+0.05 in relative coordinates). **Figure 2(a)** shows electron density differences for the A_{2u} mode looking along the *c*-axis equivalent direction and **Figure 2(b)** is the view perpendicular to the *c*-axis. **Figure 2(b)** shows that the boron planes, with the superimposed electron density difference, are closer to Mg atoms in the plane immediately above the boron plane than to the Mg plane immediately below. This outcome is also expected for the A_{2u} mode of the MgB_2 structure. The view of electron density difference along the *c*-axis (**Figure 2(a)**) shows the in-plane symmetry of MgB_2 is similar to that in **Figure 1(a)**.

Figure 3 shows the electron density difference of the E_{1u} mode for a similar level of relative displacement with (+0.05 in relative coordinates) along the direction of the B−B bond. **Figure 3** shows atom positions viewed along the *c* axis in which the Mg atoms are shifted in the direction of the arrows or approximately along <110>. In **Figure 3**, Mg atoms are closer to the B atoms of the adjacent hexagonal ring rather than symmetrically at the centre of the (001) projection in an undistorted unit cell. Nevertheless, a change in symmetry of the electron density difference on the boron plane is not detected with this imposed relative displacement of atoms along E_{1u} modes.

To illustrate the effect of an incremental increase or decrease in B−B bond length due to incremental displacement of atoms along an E_{2g} phonon mode, **Figure 4** shows the resulting electron density differences in a series of single unit cells with superimposed electron density differences (in light blue) and localization functions (in dark blue) using the same iso-value (*e.g.* 0.15) as in **Figure 1**. Scrutiny of the series of relative displacements in **Figure 4** shows that there is an asymmetric arrangement of the electron density differences and the electron

(a) (b)
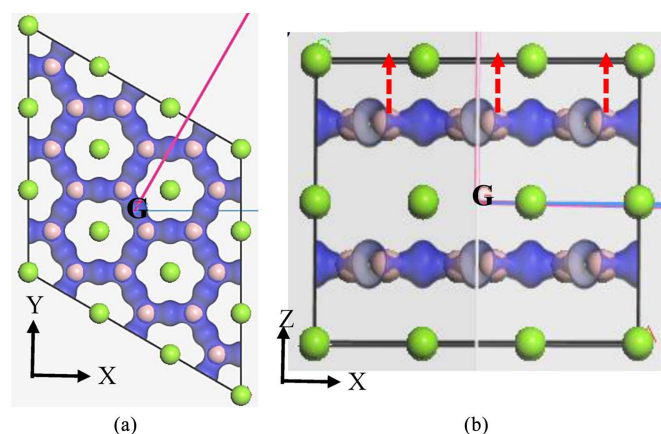
Figure 2. Electron density difference distributions (in blue) in MgB_2 for atom displacements corresponding to the A_{2u} mode; (a) viewed along the *c*-axis direction and (b) viewed along the *a*-axis direction perpendicular to (a). Red dashed arrows indicate direction of atom displacement(s).
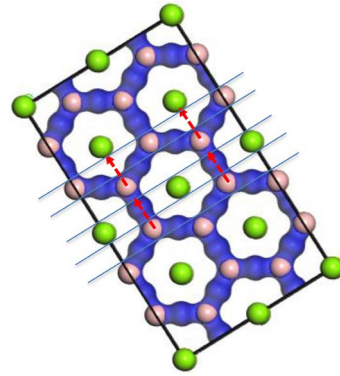
Figure 3. View along the c-axis direction of MgB$_2$ showing the electron density difference (in blue) for displacements corresponding to the E$_{1u}$ mode (red dashed arrows denote direction of displacement). Note the minor shift of Mg atoms in the direction of the displacement; light blue grid lines are guides only.
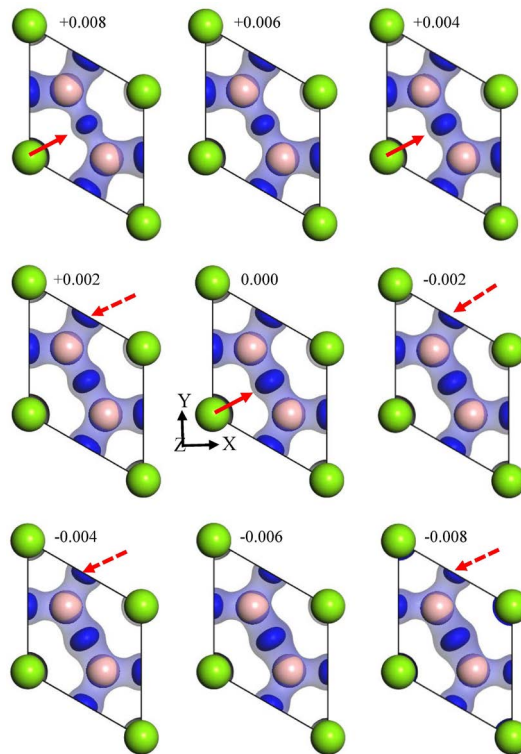
Figure 4. View along the nominal *c*-axis direction of MgB$_2$ showing the electron density difference (light blue) with superimposed electron localization functions (dark blue) for a series of incremental atom displacements corresponding to one of the E$_{2g}$ modes. The relative displacement values (D$_x$ = ±0.00 n) are enumerated for each unit cell configuration. Mg atoms are green and boron atoms are pink; red arrows are guides to regions of significant change.

localization functions which becomes more pronounced as the displacement increases from the equilibrium position (e.g. Dx = 0.00). Note that these shifts

in electron distribution are more subtle in **Figure 4** than in **Figures 1-3** because the magnitudes of the displacements are smaller.

The data in **Figure 4** show an asymmetry between the elongated and the compressed directions of the inter-bond distance. For example, in this configuration a complete B−B bond is located in the centre of the unit cell and four half-bonds (*i.e.* two net bonds) point towards the unit-cell edges. This results in an imbalanced response (by a factor of 2) to compression or extension. In compression, an increased electronic charge is established between the boron atoms within the same unit cell. When these bonds are stretched or extended, adjacent B−B bonds are compressed with a resulting build-up of equivalent increased electronic charge at the edges of the unit cell, but distributed to twice the number of bonds.

It is clear from the above analyses that the E_{2g} modes are the only modes to generate observable modulated electron density differences within the boron plane. This modelled outcome is consistent with previous experimental data and calculations that show the E_{2g} mode is strongly electron-phonon coupled and a key enabler of superconductivity in MgB_2. These electron density differences produce bond charge modulations which have super-lattice periodicities with respect to the original MgB_2 crystal. These changes reflect the effects of mobile electronic charge response along the bond direction(s) due to the changes in interatomic attractions and/or repulsions from atomic displacements induced by the E_{2g} phonons (see Discussion).

3.2. Band Structures

We have evaluated the influence of atom displacements—using similar parameters as in Section 3.1—on the electronic band structure of MgB_2. **Figure 5** shows the electronic band structures for a series of incremental changes in relative displacement from the equilibrium position that follow the movement of an E_{2g} mode along the B−B inter-bond direction. These band structures are calculated using the LDA functional with k-grid separation $\Delta k = 0.01$ A^{-1}.

With increased distance between displaced boron atoms, the primary influence on the band structures is removal of band degeneracy along the **G−A** (or **G−Z**) reciprocal direction adjacent to the Fermi level (**Figure 5**; circled). In addition, a corresponding separation of the inverted parabolas (nearly free-hole like) occurs at **G**. **Figure 5(e)** also shows that an electronic σ band (the inverted parabolas at the **G** point near the Fermi level) becomes nearly tangential to the Fermi level for the relative atom displacement $D_x = \pm 0.006$.

3.2.1. Fermi Energy

We determine the calculated Fermi energy for each model of MgB_2 with a specific deformation potential using the LDA and the GGA functionals. As is well known, the Fermi level (and energy) represents the most energetic valence electrons at 0 K which, for bands of metallic behaviour, may participate in electron transport. Only these electrons with energies within a range of k_BT, where k_B is
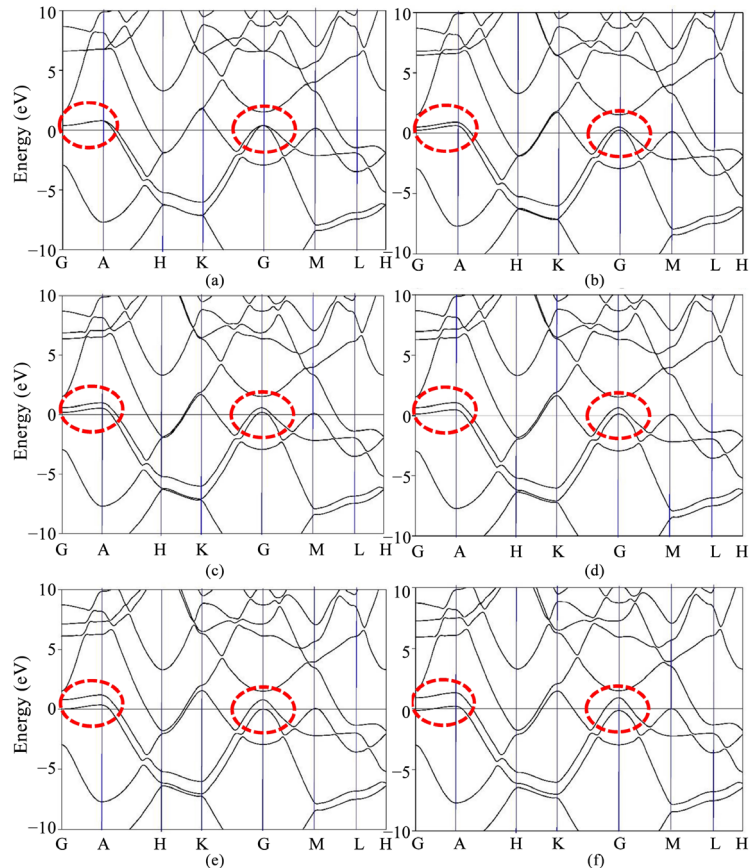
Figure 5. Electronic band structures for MgB_2 calculated using the LDA functional with B–B atom displacements along an E_{2g} direction corresponding to (a) $D_x = 0.0$; (b) $D_x = -0.002$; (c) $D_x = -0.003$; (d) $D_x = -0.004$; (e) $D_x = -0.006$ and (f) $D_x = -0.008$. Note that for a displacement around -0.006, the lower parabolic branch of the electronic band at **G** becomes tangential to the Fermi level, and for -0.008 this branch is already below the Fermi level.

Boltzmann's constant and T is temperature, participate in electronic transport properties at the Fermi energy. Use of DFT with a consistent approach and software suite can provide accurate values of the Fermi energy for MgB_2 and similar structures with reference to the total number of valence electrons. Note that some earlier computational studies choose to denote a reference point for the Fermi energy at different values to that used in this and our earlier studies [4] [5], closer to the top of the valence band, emphasizing the hole nature of the charge carriers.

Nevertheless, the analysis in this paper shows differences of many meV with atom displacement from the equilibrium position. This change in Fermi energy as a function of the relative atom displacement coordinates for both LDA and GGA approximations are shown graphically in **Figure 6**. Further detail on the form of this variation in Fermi energy with atom displacement is shown in the enlarged view of **Figure 6(b)**, calculated with the LDA functional at the same resolution as **Figure 6(a)** for $\Delta k = 0.01$ A^{-1}. We also present a summary of bond
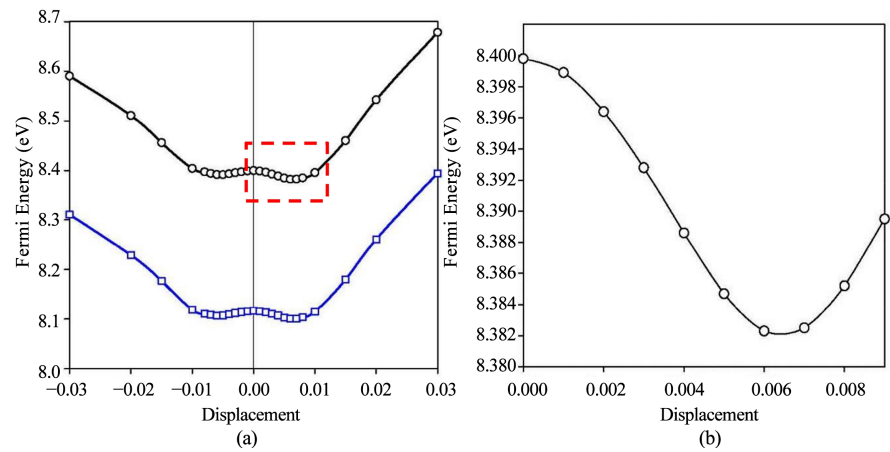
Figure 6. (a) Fermi energies using the LDA and GGA functionals with Δk = 0.01 A^{-1} (and lattice expansion factor 1.000x) for MgB$_2$ with various displaced B–B bond distances; (b) Enlarged view of the Fermi energies in the region within the red dotted rectangle. These data are obtained using the LDA functional calculated at a k-grid, Δk = 0.01 A^{-1}.

lengths and Fermi energy determined with the LDA functional for a range of atom displacements and for a lattice expansion of 1.006x in **Table 1**. This factor of 1.006x is an approximation to an isotropic expansion of the entire lattice (or unit cell) equivalent to ~40 K. In contrast, an expansion factor of 1.000x represents lattice parameters optimised for absolute zero temperature.

Figure 6 shows that the variation of calculated Fermi energies using the LDA and GGA approximations are similar in form and appearance but with a difference in energy of ~0.38 eV. In all other respects, the curves for both calculations are identical. In both cases, the Fermi energy displays local minima at relative displacements of about $D_x = \pm 0.006$ and a local maxima at the equilibrium position ($D_x = 0.000$). The depth of the energy minimum at the elongated position ($D_x = +0.006$) is approximately two times the value of the energy minimum at the contracted position ($D_x = -0.006$). The difference in Fermi energies between the elongated minimum and the equilibrium position is ~17.5 meV and 15.9 meV, for lattice expansion factors 1.000x and 1.006x, respectively. These values, particularly the difference for the lattice expanded by 1.006x, are comparable to two times the value of the MgB$_2$ superconducting gap [25] [26]. The differences in Fermi energies for the contracted and elongated displacements appear related to the number of contracted bonds identified in **Figure 4**.

3.2.2. Fermi Surface

The widely accepted topology of the MgB$_2$ Fermi surface consists of coaxial, nearly parallel "tubular" sections for σ bands in the *c* axis direction and three dimensional interconnected bands [27]. These tubular sections resemble an hourglass shape and are also referred to as warped cylinders [28]. Fermi surfaces provide a three dimensional, iso-value representation in reciprocal space of the Fermi energy. We have calculated the changes in Fermi surface for MgB$_2$ with

Table 1. Parameters for MgB$_2$ calculated using the LDA functional.

D$_x$ (fractional coordinates*)	B–B distance (Å)	0K Energy (eV)	Fermi Energy (eV)
Lattice expansion factor = 1.000			
0.000	1.755	−1748.5005	8.3998
0.001	1.766	−1748.5003	8.3989
0.002	1.776	−1748.4995	8.3965
0.003	1.781	−1748.4980	8.3928
0.004	1.797	−1748.4957	8.3886
0.005	1.808	−1748.4928	8.3847
0.006	1.818	−1748.4894	8.3823
0.007	1.829	−1748.4856	8.3825
0.008	1.839	−1748.4815	8.3852
0.009	1.850	−1748.4769	8.3895
Lattice expansion factor = 1.006			
0.000	1.7657	−1748.4955	8.2149
0.001	1.776	−1748.4953	8.2141
0.002	1.787	−1748.4945	8.2119
0.003	1.797	−1748.4932	8.2087
0.004	1.808	−1748.4912	8.2048
0.005	1.819	−1748.4885	8.2011
0.006	1.829	−1748.4853	8.1990
0.007	1.840	−1748.4819	8.1995
0.008	1.850	−1748.4781	8.2027
0.009	1.861	−1748.4739	8.2074

*From geometry optimized relative coordinates (0.3333, 0.6666, 0.5).

incremental increase in atom displacement from the equilibrium position. These Fermi surfaces are shown for calculations using the LDA functional with Δk = 0.01 A^{-1} in Figure 7.

At small atom displacements, the Fermi surface shows a familiar coaxial warped tubular section consistent with previous calculations [2] [28]. With an increase in the relative displacement of atom(s), the internal warped tubular cylinder shows a reduced radius which is exaggerated at the reciprocal lattice origin, **G**. With further increase in atom displacement, this feature manifests as "necking" in the centre of the cylinder at **G** as shown in Figures 7(b)-(c). Ulti-

mately, the Fermi surface collapses into a thin line at the mid-point of the reciprocal cell when the relative atom displacement, $D_x = -0.006$ as shown in **Figure 7(c)**. This relative atom displacement is the point at which the corresponding σ band becomes almost tangential to the Fermi level as identified in **Figure 5**. With further atom displacement, the σ Fermi surface breaks apart into two approximate paraboloid sections that face in opposite directions as shown in **Figure 7(d)**.

Parallel warped tubes coaxial with the *z*-direction shown in **Figure 7(a)** correspond to the heavy (outer tube) and light (inner tube) effective mass σ bands. The light effective mass σ band displays a topological transition to separate paraboloid sections facing in opposite directions (**Figure 7(d)**) as the B-B distance is gradually increased (or decreased) about 0.6% in relative coordinates. Other Fermi surfaces near the surrounding Brillouin zone boundaries do not change significantly and correspond to the π bands.

3.3. Phonon Dispersions

We have utilized the phonon dispersion (PD) in previous computational analyses to illustrate the strong link between optical phonon behaviour and band structure in MgB_2 [5]. We have also shown that the depth of the PD anomaly provides a temperature which corresponds to the superconducting transition temperature for a wide range of external conditions, accurate within experimental and calculation errors [5] [6] [7] [14]. Consistent with this approach, we also
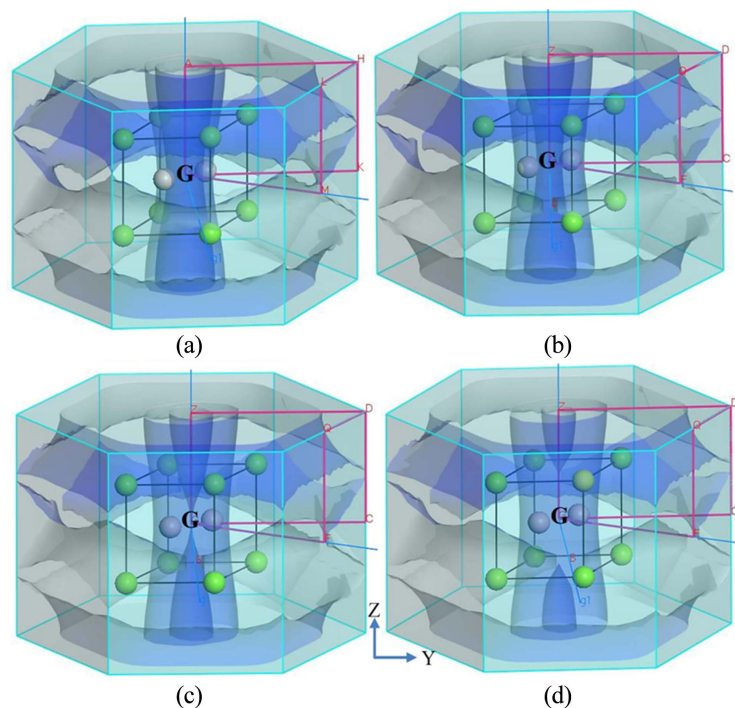
Figure 7. Fermi surfaces of MgB_2 calculated with LDA for $\Delta k = 0.01\ A^{-1}$ with various displaced B−B bond distances: (a) $D_x = -0.002$; (b) $D_x = -0.004$; (c) $D_x = -0.006$ and (d) $D_x = -0.008$.

highlight in **Figure 8** the influence of incremental atom displacements on specific phonon modes. As noted in earlier work, PD calculations are computationally intensive [5] [7]. Hence, this evaluation of atom displacements is performed using the LDA functional with fewer sampling points and limited reciprocal space directions (*e.g.* along **G−M**, **G−K** and **G−A** only). **Figure 8** shows the changes in PD modes for **G−M** and **G−K** reciprocal directions with particular emphasis on the E_{2g} phonon with increase in relative atom displacement from the equilibrium position.

Figure 8 shows significant change in the form of the E_{2g} phonon anomaly with increased atom displacement from equilibrium and an increase in energy of one of the degenerate modes at **G**. At large atom displacement (*e.g.* $D_x = 0.008$; **Figure 8(d)**), the E_{2g} phonon anomaly (below the B_{2g} mode) is absent and the order of modes (*i.e.* relative energy or frequency) is reversed between the B_{2g} and E_{2g} phonons. Evaluation of the band structures in **Figure 5** shows a corresponding change in form of a σ electronic band branch which shifts below the Fermi level. This feature also corresponds with changes in the Fermi surface as shown in **Figure 7** where, at relative displacement $D_x = 0.008$, the surface becomes two separate paraboloids. These computational outcomes further confirm the strong link between the electronic bands, Fermi surface nesting and the depth of the PD anomaly. These inter-relationships are clearly associated with the superconducting transition temperature for AlB_2-type structures [4] [5] [6] [7] [29].
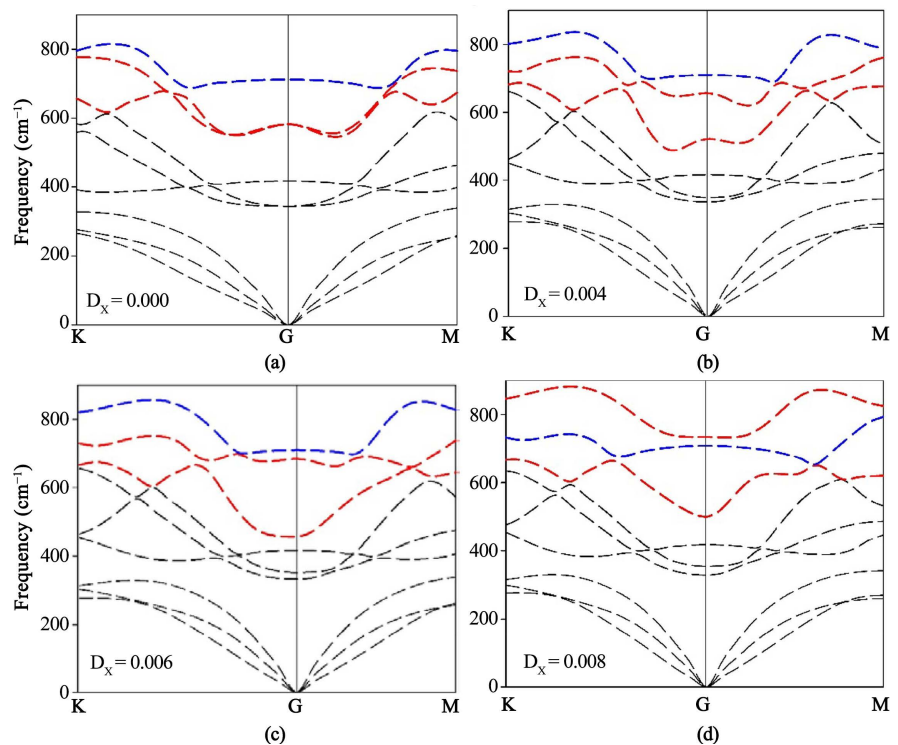
Figure 8. Phonon dispersion plots for MgB_2 calculated with the LDA functional for $\Delta k = 0.01 \ A^{-1}$ and primitive symmetry for various displaced B−B bond distances: (a) $D_x = 0.000$; (b) $D_x = 0.004$; (c) $D_x = 0.006$ and (d) $D_x = 0.008$. E_{2g} vibration modes are in red; B_{2g} modes are in blue.

4. Discussion

In earlier publications, we utilize *ab initio* DFT to recognize the shape and extent of the E_{2g} phonon anomaly in MgB_2 [4] [5] as well as in metal-substituted MgB_2 [5] [7] and MgB_2 under the influence of hydrostatic pressure [6]. In each of these studies, we compare computational outcomes with experimental data to show that the phonon dispersion (PD) is an effective tool for recognition of a phonon anomaly and that the thermal energy of this anomaly is correlated with the experimentally determined value of T_c for the superconducting transition of MgB_2 compounds. This approach—based primarily on calculated PDs—is extended to other AlB_2-type compositions [5] and is also the basis for prediction of new compounds that are likely to be superconductors [5] [7].

As is well-known, a strong crystallographic link exists between band structure calculations and PD models based on DFT. This link between phonon behaviour and electronic band structure requires fine k-grid resolution and thus high computational cost to elucidate PD data [5] [7]. However, MgB_2 offers an ideal structural format to highlight this link between electron and phonon behaviour consistent with the well understood view of electron-phonon coupling as key to conventional superconductivity [30]. A connection between the E_{2g} phonon and the Fermi surface as well as components of the E_{2g} phonon anomaly with the band structure at or near **G** is described for MgB_2 [5] [6] and more recently, elucidated by experiment [31] using Inelastic X-ray Scattering (IXS). In this work, we elaborate further on the interaction between the electronic band structure and phonon behaviour of MgB_2, in particular, as revealed by electron density difference distributions in response to deformation potentials.

4.1. Fermi Energy

Born and Oppenheimer introduced the adiabatic approximation, in which electrons are expected to move much faster than heavier nuclei, allowing for a very rapid redistribution of electronic charge, every time a nuclei undergoes movement [32] [33]. This assumption allows for substantial separation of nuclear and electronic coordinates while solving the Schrodinger equation [33]. As pointed out by Boeri *et al.* [34], the Born-Oppenheimer approximation is implicitly assumed in DFT, whereby the electron density distribution can be calculated for each ionic configuration. According to Uchiyama *et al.* [35] the close agreement between DFT calculated electronic bands and Angle Resolved Photoemission (ARPES) data up to binding energies as high as 2.5 eV suggests that electronic correlations in MgB_2 are unimportant. As a result, they contend that this material is well described by conventional band theory [35].

Boeri *et al.* [34] argue against the validity of the adiabatic approximation for MgB_2, based on an abnormally small (~0.5 eV) Fermi energy (E_F) calculated for the σ bands, assumed to be of the same order as the highest phonon energies. However, the Fermi energy assigned by Boeri *et al.* [34] appears related to the distance to the vertex of the parabolic bands and does not correspond to valence

electron densities or charge carriers determined experimentally from resistivity measurements and from Drude approximations. For example, measurements of the Hall coefficient for MgB_2, indicate that the charge carriers are holes with a density of 1.7 - 2.8 × 10^{23} holes cm^{-3} at 300 K [27] [36] [37]. In contrast, calculations by Suzuki [38], referred to the vertex of the parabolic bands, estimate a carrier concentration of ~10^{22} holes cm^{-3} an order of magnitude different to experiment.

The disparity between calculated Fermi energy and experimental measurements—albeit indirect—appears in many publications that refer the energies to the top of the valence bands and reset the reference Fermi level to zero energy. We consider this disconnect between the absolute Fermi energy values calculated by DFT (from the total number of available valence electrons and states) and the traditional "zeroing" of the reference level to cause loss of valuable insight and to be a source of potential confusion in the literature. A critical factor for this work, and others requiring similar detail and accuracy, is that the topologies of Fermi surfaces are determined by the absolute calculated Fermi energy with respect to Brillouin zone dimensions, where valence states are essentially filled with the total number of valence electrons (with a two times division to account for spin directions in spin unpolarized calculations). This change in reference point for the Fermi energy, combined with aggregation of information in reduced Brillouin zone schema in reciprocal space lead to complications with interpretation as outlined in the next section.

The calculated Fermi energies for a range of configurations in MgB_2, presented in Table 1 are consistent with earlier DFT models for metal substituted or pressure dependent forms [5] [6] [7]. DFT calculations for MgB_2 using CASTEP in Materials Studio result in a Fermi energy of 8.3998 eV and 8.1165 eV using the LDA and GGA approximations, respectively. The results from CASTEP are more consistent with the high carrier densities determined from Hall effect measurements [27] [36] [37]. Thus, we consider that the absolute value of Fermi energy ranges between 8.1 eV and 8.4 eV as consistently demonstrated in a number of DFT computations undertaken previously [5] [6]. The insight we learn from *ab initio* DFT is that choice of appropriate functionals and proper account of valence electron numbers help elucidate the strong correlation between electronic, vibrational and superconducting properties for MgB_2. Furthermore, we argue that the adiabatic approximation is a justifiable assessment for MgB_2 for a wider range of conditions than previously considered.

4.2. Fermi Surfaces, Phonons and Gap Values

The Fermi surface separates the filled electronic states from the empty electronic states in three-dimensional reciprocal space at absolute zero temperature [39]. The widely accepted topology of the MgB_2 Fermi surface consists of coaxial, nearly parallel "tubular" sections for σ bands in the c axis direction [27]. The outer and inner tubular sections for MgB_2 correspond to the heavy and light ef-

fective masses for the σ bands, respectively [2] [28] [40]. The hole nature of the tube implies that at absolute zero temperature the inside of the tube is empty and the outside of the tube is filled. This requires that in an extended zone scheme, tubular Fermi surfaces should be located away from the origin, possibly at the corners or outside the first Brillouin zone. Referral of the Fermi energy to the vertex of the approximate parabolic σ bands may unnecessarily confuse interpretation of electronic parameters and construction of Fermi surface topologies in this structure and others. Apparent confusion in the literature arises because in graphic representations, boundaries for Fermi surfaces are displayed without a clear delineation of where electrons and empty states, respectively, reside.

Furthermore, two parallel tubular Fermi surfaces also create a dilemma when the two tubes are represented in a coaxial fashion. This is because at zero temperature, in the volume between these two surfaces, electrons occupy energy levels outside the inner light effective mass tubular section, while empty states with identical magnitude of momentum and energy exist inside the outer, heavy effective mass tubular section [27] [30]. We suggest that this dilemma is, in practical terms, resolved via the schematic shown in **Figure 9** for the coaxial σ Fermi surfaces of MgB$_2$. In this schematic, we neglect the warping of the σ Fermi surfaces as previously described [6].

In the reduced zone scheme of the Brillouin zone, the inter-tube volume is an important region where levels close to the Fermi energy with identical **k**-vectors plus or minus a reciprocal space **G** vector (and similar energy) show filled character
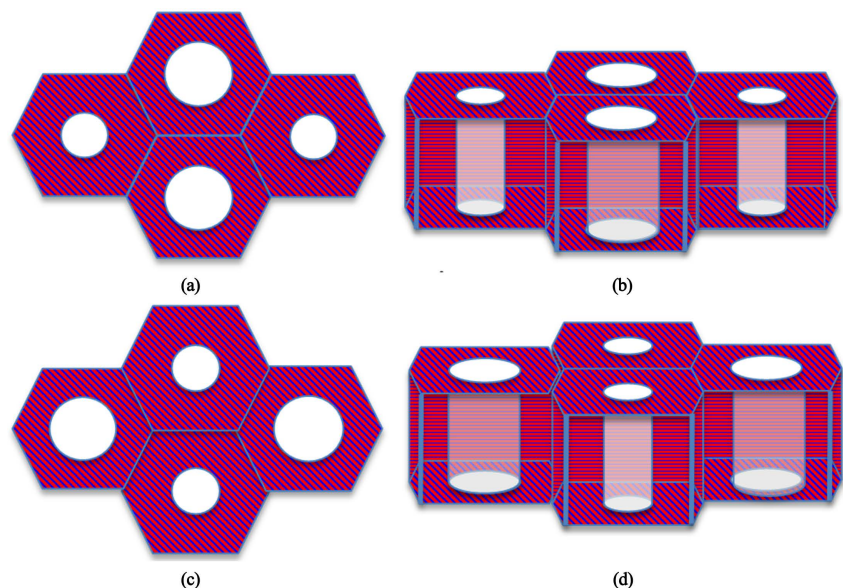
Figure 9. Idealised schematic of the σ Fermi surfaces for MgB$_2$ represented in an extended Brillouin zone schema viewed (a) down the *c*-axis and (b) perspective view at an angle to the *c*-axis; (c) and (d) show equivalent resonant states for (a) and (b) relative to the reciprocal space vector **G**. Warping of the σ Fermi surfaces is neglected in this schematic.

relative to the light effective mass, but an empty character relative to the heavy effective mass [6]. We assume that a reduced zone representation, in essence, aggregates tubes of different diameter that occur at different places in an extended Brillouin scheme, connected by reciprocal space $\mathbf{G}$ vectors. Therefore, we infer that an extended zone scheme explicitly manifests a resonating behaviour between the tubes at different reciprocal space locations (shown in Figure 9) [6] and may be a more appropriate representation of these states compared with a reduced zone schematic.

We have previously shown that the apparent inter-tubular volume controls the depth of the phonon dispersion anomalies in AlB_2-type structures [5] [7]. We have also demonstrated a correlation between a temperature associated with the PD anomaly (*i.e.* T_δ) and T_c, and, as an extension of this phenomenom, propose that this inter-tubular volume is a key region in reciprocal space for superconductivity. As pointed out by Geballe *et al.* [3], T_c itself and its response to controlled changes in external parameters, often help reveal the responsible mechanisms for superconductivity. Given the excellent correlation between the depth of PD anomalies, Fermi surfaces and T_c, it appears that useful insights on superconducting mechanisms are hidden within these inter-tubular Fermi surface constructs.

4.3. Dynamic Fermi Surfaces and Bond Charge Modulations

Figure 8 shows a clear transition of Fermi surfaces with increased atom displacement from the equilibrium position for MgB_2. This transition involves the collapse of one σ Fermi surface as the B−B distances are displaced relative to the equilibrium value. This transition also corresponds to a disruption of the coherent interconnection, or nesting, between the two tubular sections. When these tubes are parallel, the hole/electron states are at exactly the same $\mathbf{k}$-point plus or minus a reciprocal space vector $\mathbf{G}$ and similar energy for the separate light and heavy mass surfaces. These filled/vacant electron states can be nested by phonons of the exact same magnitude. However, once one surface collapses, this perfect nesting is disrupted and the model suggests that this is when the superconducting T_c is breached. This modelling also suggests that the condition at which these tubular sections cannot be connected by the same magnitude phonon may signal the beginning of incoherent scattering in MgB_2.

The form of parallel Fermi surfaces shown in Figure 9 (and, more precisely, in Figure 7) are similar to the ideas and figures discussed by Bardeen (Figure 1 in ref [41]). In Bardeen's article, a shell structure around the Fermi surface is identified as the region of electron states that are important for superconductivity. The Fermi surface of MgB_2 for significantly displaced boron atoms is also similar to the effect of Al substitution in $Mg_{1-x}Al_xB_2$ [42] (compare Figure 7 of this work with Figure 4 of [42]). Both results show an evolution to a topology with two separate cusps, with corresponding degradation of superconducting properties.

However, Fermi surfaces described by de la Peña *et al.* [42] consist of two

separate sets of cusps that retain similar parallel shapes. In contrast, and as shown in Figure 7, after the critical displacement or separation of boron atoms is achieved (at relative displacement $D_x = \pm 0.006$), one surface completely collapses and the remaining Fermi surface cusps consist of single surfaces. Alternatively, we may consider that as the temperature is lowered towards the superconducting transition temperature, the mixed topology of parabolic cusps and tubular sections is interacting more strongly and evolving into the set of approximately parallel tubular sections. This interpretation would then be more in-line with important concepts proposed earlier on topological transitions that determine or enhance T_c [14] [15] [43].

Figures 4-8 also highlight the duality of real and reciprocal space interactions between Fermi energy, phonon frequencies and electron density. This duality is because of a direct connection to the directional bond charge distribution that modulates the repulsive B−B forces determining the key E_{2g} phonon frequencies and the apparent strong localization of the electron density at the Fermi energy along the highly covalent B−B bonds. Similar undulating shapes of the PD curves [4], and the dependence of the Fermi energy on the relative atom displacement shown in Figure 6 reflects this duality.

The E_{2g} frequency of the appropriate branch increases as the B−B distance is displaced from the equilibrium position. The simultaneous drop in the Fermi energy seems to account for the energy that is passed onto the generated phonons, as a result of an electron jumping to alternative bonds responsible for the modified electron density differences (see Figure 4 and Figure 6). In the PD, this manifests as a higher E_{2g} frequency with an associated reduced PD anomaly. Once the displacement exceeds the "gap" limit, it will generate such energetic phonons that other modes become involved and the system cannot maintain coherency. A mechanical analogy to this condition is as if a natural spring is overstretched and then released, causing a disturbed movement back to the equilibrium position.

A schematic of the bond charge modulation pattern in the boron plane of MgB_2 is shown in Figure 10. The charge modulation has a complex pattern that only appears as the atoms deviate from their equilibrium positions. As the restoring forces bring atoms back to their equilibrium positions, the modulated charge pattern disappears. The dynamic origin of the bond charge modulation observed in MgB_2 may be different to that of a standard charge density wave (CDW) because of the specific crystallography of the structure. The restoring forces from phonons or lattice vibrations are poised to re-equilibrate geometrical and electronic structures to no modulation. For motion in the reverse direction, a new electron density difference is generated and then disappears in a resonant fashion. In a CDW, charge modulation is expected to be more persistent or permanent, since its manifestation is more prevalent as determined *via* a wide range of experimental characterization techniques. Nevertheless, this work may shed light on geometrical relationships between nesting vectors (in reciprocal space) and bond charge modulation (in real space) [44].
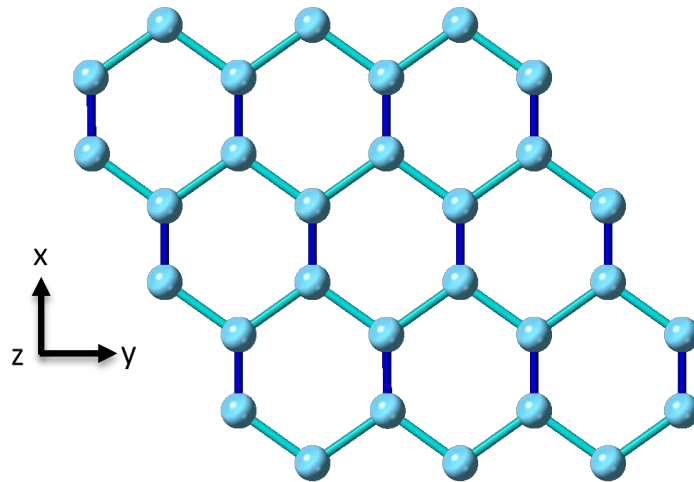
Figure 10. Schematic of the bond charge modulation pattern in the boron plane of MgB_2 based on DFT calculations for displaced atom configurations. Blue spheres represent boron atoms; dark blue bonds represent regions of higher electron density and light blue bonds represent lower electron density. Distortion along the x direction (equivalent to an E_{2g} mode direction) for the average hexagonal unit cell is accentuated in this schematic.

The schematic in **Figure 10** also reveals that modulated bond charge distributions can be largely represented by net dipolar contributions, if not collectively, at least at the local scale. The alternating dark blue and light blue bonds between boron atoms in the *a-b* plane represent locally enhanced (positive) and reduced (negative) electron densities at the largely covalent B–B bonds (see also **Figure 1** and **Figure 4**).

4.4. Temperature Dependent Mechanism

Two of the most direct manifestations of temperature effects on the geometrical structure that can be measured are the thermal expansion and the temperature dependence of lattice parameters. Both thermal expansion and changes in lattice parameters with temperature have been investigated for MgB_2 [45] [46] [47] [48] [49]. Thermal expansion is modest or even negative before and soon after the superconducting transition temperature, but develops a much sharper and linear increase at higher temperatures. The change in lattice parameters with temperature follows a similar pattern. Detailed neutron refinement investigations by Jorgensen *et al.* [45], provide Debye Waller factors and mean square atomic displacements over a wide temperature range for MgB_2.

Our atom displacement calculations impose an increasing change in the B–B inter-bond distance from the equilibrium distance. This approach indirectly mimics the effect of increased temperature on this inter-bond distance. For example, the mean square displacement for boron at 37 K [45] is measured as U_{11} = 0.00333 (11) Å^2, U_{33} = 0.00455 (18) Å^2 and U_{12} = 0.00166 (6) Å^2. The square roots of these values are 0.0577 (10) Å, 0.0674 (13) Å and 0.0407 (7) Å, respec-

tively. If we compare these values to the difference in B–B bond distance at equilibrium and at a relative displacement $D_x = \pm 0.006$ at the transition temperature (~39.4 K), we obtain 0.0631 Å (= 1.7551 - 1.6920) and 0.064 Å (= 1.7782 - 1.7142) for the LDA and GGA functionals. This relative displacement is for an expansion factor of 1.000x in all three real space directions. These calculated values display good correspondence with the square root of the mean square displacement for boron at 37 K based on precise experimental data [45]. Therefore, our assumption that a relative displacement of $D_x = \pm 0.006$ corresponds approximately to the superconducting transition temperature (~39.4 K) is reasonable given the relative errors in calculations and in experimental measurements. The estimated inter-bond displacement required for collapse of superconductivity is consistent with experimental measurements of the square root of the mean square displacements by Jorgensen *et al.* [45]. This consistency between theory and experiment further supports our suggestion that these calculated effects are directly linked to temperature.

A critical, and perhaps unique, aspect of superconductivity in MgB_2 is that electron density differences and phonon modes are largely confined to the *a-b* plane. This configuration allows a direct correlation of DFT calculations to key properties in the structure. This computational approach highlights that the electron density difference responds to increased atom-atom repulsion as the distance between atoms is reduced. As a result, an increased electronic bond charge is required to minimize the overall energy. These bond charges are localized along the highly covalent inter B–B bond distances, and along with a phonon mode that is oriented along the same direction, seem to moderate the correlation. The proportion of transferred charge density directly affects the Coulomb repulsions and can translate into a net force change. This net force is related to a change in the magnitude of the phonon frequency.

We note that other, more complex structures may not show phonon modes with movement aligned to a specific inter-bond distance. In such a case, more than one phonon may influence electron density differences for a particular bond direction with resulting complex patterns of electron density differences and phonon displacements. In addition, magnetic interactions may also add to the force constants with consequent influence on interatomic distances and displacement patterns. Not all of the structures will exhibit a situation equivalent to the important interplay of approximately parallel σ bands and maintain coherency as electron density differences minimize the energy in response to the atom movements along specific phonon modes. However, the existence of parallel tubular Fermi surfaces, coaxial in a reduced Brillouin zone scheme, is ubiquitous to all layered superconductors. This phenomenom may hide important information about superconductivity which may require disaggregation to improve our understanding for effective materials design. Given the accurate validation of these calculations for a range of external conditions, we propose that this approach may be valid for many other examples of superconductivity.

5. Conclusions

The Fermi energy of the valence electrons in MgB_2 is sufficient to justify the adiabatic or Born-Oppenheimer approximation in quantum mechanics calculations for MgB_2. In this work, we present a model that identifies the distribution of electrons and empty states on the MgB_2 Fermi surface and, through this, a mechanism associated with the inter-tubular volume between the σ Fermi surfaces that tracks the onset (or demise) of superconductivity.

The net volume enclosed between the parallel heavy and light effective mass σ Fermi surfaces when represented in the reduced Brillouin zone is an important region of reciprocal space for superconductivity. This region, when represented in an extended zone (e.g. **Figure 10**; [6]) is suitable for a resonant interaction between separate heavy and light hole Fermi surfaces. This inter-surface region is also ideal for nesting to occur between different sections of the Fermi surface, by a phonon vector of constant magnitude, within a thermal energy range k_BT from the Fermi energy. Analysis of frozen, displaced boron atoms along the B−B inter-bond distance confirms that the phonon anomaly collapses as the inter-bond distance increases. The variation of Fermi energy for displacements along the E_{2g} phonon mode that stretches or contracts along the inter-bond distance is smooth and accounts for changes in the electronic charge density along predominantly covalent B−B bonds, which reduces the overall energy by neutralizing increased atomic core repulsions.

The difference between the Fermi energy at a critical displacement of ~0.6% ($D_x = \pm0.006$) in relative coordinates and the Fermi energy at the equilibrium position displays a strong correlation to the superconducting energy gap, or multiples of the gap, depending on the number of bonds that are involved in electron density transfer. Our analysis of the shift in E_{2g} and B_{2g} PD bands with atom displacement suggests that the interplay between potential energy and kinetic (or thermal) energy stored in the inter-bond distance is a key determinant of T_c in AlB_2-type materials. This analysis of displaced atomic positions also highlights that the Fermi surface is time dependent and dynamic in character. The dynamic character of the Fermi surface is not only important for an understanding of superconductivity, but also for many other electronic properties.

Earlier studies using McMillan equations, invoked normal state parameters to explain or predict T_c, and, consistent with this, DFT is a tool that provides all necessary information to understand superconductivity in AlB_2-type structures. Phonon dispersion (PD) calculations shown in this work linked to band structure calculations via DFT, is an effective, reliable and consistent method to accurately determine a temperature strongly correlated with the superconducting T_c of an AlB_2-type material from knowledge of the crystal structure.

Acknowledgements

with, QUT's HPC facilities particularly from Ashley Wright and Abdul Sharif, is gratefully acknowledged.

References

[1]   Kohn, W. (1999) Nobel Lecture: Electronic Structure of Matter—Wave Functions and Density Functions. *Reviews of Modern Physics*, **71**, 1253-1266. https://doi.org/10.1103/RevModPhys.71.1253

[2]   An, J.M. and Pickett, W.E. (2001) Superconductivity of MgB_2: Covalent Bonds Driven Metallic. *Physical Review Letters*, **86**, 4366-4369. https://doi.org/10.1103/PhysRevLett.86.4366

[3]   Geballe, T.H., Hammond, R.H. and Wu, P.M. (2015) What T_c Tells. *Physica C: Superconductivity and Its Applications*, **514**, 9-16. https://doi.org/10.1016/j.physc.2015.02.009

[4]   Alarco, J.A., Chou, A., Talbot, P.C. and Mackinnon, I.D.R. (2014) Phonon Modes of MgB_2: Super-Lattice Structures and Spectral Response. *Physical Chemistry Chemical Physics*, **16**, 24443-24456. https://doi.org/10.1039/C4CP03449J

[5]   Alarco, J.A., Talbot, P.C. and Mackinnon, I.D.R. (2015) Phonon Anomalies Predict Superconducting T_c for AlB_2-Type Structures. *Physical Chemistry Chemical Physics*, **17**, 25090-25099. https://doi.org/10.1039/C5CP04402B

[6]   Alarco, J.A., Talbot, P.C. and Mackinnon, I.D.R. (2017) Phonon Dispersion Models for MgB_2 with Application of Pressure. *Physica C: Superconductivity and Its Applications*, **536**, 11-17.

[7]   Mackinnon, I.D.R., Talbot, P.C. and Alarco, J.A. (2017) Phonon Dispersion Anomalies and Superconductivity in Metal Substituted MgB_2. *Computational Materials Science*, **130**, 191-203. https://doi.org/10.1016/j.commatsci.2017.01.011

[8]   Zheng, J.-C. and Zhu, Y. (2006) Searching for a Higher Superconducting Transition Temperature in Strained MgB_2. *Physical Review B*, **73**, Article ID: 024509. https://doi.org/10.1103/PhysRevB.73.024509

[9]   Nagamatsu, J., Nakagawa, N., Muranaka, T., Zenitani, Y. and Akimitsu, J. (2001) Superconductivity at 39K in Magnesium Diboride. *Nature*, **410**, 63-64. https://doi.org/10.1038/35065039

[10] Kunc, K., Loa, I., Syassen, K., Kremer, R.K. and Ahn, K. (2001) MgB_2 under Pressure: Phonon Calculations, Raman Spectroscopy, and Optical Reflectance. *Journal of Physics: Condensed Matter*, **13**, 9945-9962. https://doi.org/10.1088/0953-8984/13/44/310

[11] Heid, R., Bohnen, K.-P. and Renker, B. (2002) Electron-Phonon Coupling and Superconductivity in MgB_2 and Related Diborides. *Advances in Solid State Physics*, **42**, 293-305. https://doi.org/10.1007/3-540-45618-X_23

[12] Baron, A.Q.R., Uchiyama, H., Tsutsui, S., Tanaka, Y., Ishikawa, D., John, J.P., Sutter, P., Lee, S., Tajima, S., Heid, R. and Bohnen, K.-P. (2007) Review: Phonon Spectra in Pure and Carbon Doped MgB_2 by Inelastic X-Ray Scattering. *Physica C: Superconductivity*, **456**, 83-91. https://doi.org/10.1016/j.physc.2007.01.028

[13] Kortus, J. (2007) Current Progress in the Theoretical Understanding of MgB_2. *Physica C: Superconductivity*, **456**, 54-62. https://doi.org/10.1016/j.physc.2007.01.023

[14] Alarco, J.A., Talbot, P.C. and Mackinnon, I.D.R. (2018) A Complete and Accurate Description of Superconductivity of AlB_2-Type Structures from Phonon Dispersion Calculations. *Journal of Superconductivity and Novel Magnetism*, **31**, 727-731.

[15] Innocenti, D., Valletta, A. and Bianconi, A. (2011) Shape Resonance at a Lifshitz Transition for High Temperature Superconductivity in Multiband Superconductors. *Journal of Superconductivity and Novel Magnetism*, **24**, 1137-1143. https://doi.org/10.1007/s10948-010-1096-y

[16] Clark, S.J., Segall, M.D., Pickard, C.J., Hasnip, P.J., Probert, M.I.J., Refson, K. and Payne, M.C. (2005) First Principles Methods Using CASTEP. *Zeitschrift für Kristallographie—Crystalline Materials*, **220**, 567-570. https://doi.org/10.1524/zkri.220.5.567.65075

[17] Refson, K., Tulip, P.R. and Clark, S.J. (2006) Variational Density-Functional Perturbation Theory for Dielectrics and Lattice Dynamics. *Physical Review B*, **73**, Article ID: 155114. https://doi.org/10.1103/PhysRevB.73.155114

[18] Hinks, D., Claus, H. and Jorgensen, J. (2001) The Complex Nature of Superconductivity in MgB_2 as Revealed by the Reduced Total Isotope Effect. *Nature*, **411**, 457-460. https://doi.org/10.1038/35078037

[19] Lee, S., Mori, H., Masui, T., Eltsev, Y., Yamamoto, A. and Tajima, S. (2001) Growth, Structure Analysis and Anisotropic Superconducting Properties of MgB_2 Single Crystals. *Journal of the Physical Society of Japan*, **70**, 2255-2258. https://doi.org/10.1143/JPSJ.70.2255

[20] Becke, A.D. and Edgecombe, K.E. (1990) A Simple Measure of Electron Localization in Atomic and Molecular Systems. *The Journal of Chemical Physics*, **92**, 5397-5403. https://doi.org/10.1063/1.458517

[21] (2002) Electron Localizability. http://www2.cpfs.mpg.de/ELF/index.php

[22] Liu, A.Y., Mazin, I.I. and Kortus, J. (2001) Beyond Eliashberg Superconductivity in MgB_2: Anharmonicity, Two-Phonon Scattering, and Multiple Gaps. *Physical Review Letters*, **87**, Article ID: 087005. https://doi.org/10.1103/PhysRevLett.87.087005

[23] Kortus, J. http://www.physik.tu-freiberg.de/~kortus/kortus-research.html

[24] Yildirim, T. http://www.ncnr.nist.gov/staff/taner/mgb2/

[25] Bugoslavsky, Y., Miyoshi, Y., Perkins, G., Berenov, A., Lockman, Z., MacManus-Driscoll, J., Cohen, L., Caplin, A., Zhai, H. and Paranthaman, M. (2002) Structure of the Superconducting Gap in MgB_2 from Point-Contact Spectroscopy. *Superconductor Science and Technology*, **15**, 526. https://doi.org/10.1088/0953-2048/15/4/308

[26] Buzea, C. and Yamashita, T. (2001) Topical Review—Review of the Superconducting Properties of MgB_2. *Superconductor Science and Technology*, **14**, R115-R146. https://doi.org/10.1088/0953-2048/14/11/201

[27] Choi, H.J., Roundy, D., Sun, H., Cohen, M.L. and Louie, S.G. (2002) The Origin of the Anomalous Superconducting Properties of MgB_2. *Nature*, **418**, 758-760. https://doi.org/10.1038/nature00898

[28] Kong, Y., Dolgov, O.V., Jepsen, O. and Andersen, O.K. (2001) Electron-Phonon Interaction in the Normal and Superconducting States of MgB_2. *Physical Review B*, **64**, Article ID: 020501.

[29] Alarco, J.A., Talbot, P.C. and Mackinnon, I.D.R. (2014) Coherent Phonon Decay and the Boron Isotope Effect for MgB_2. *Physical Chemistry Chemical Physics*, **16**, 25386-25392. https://doi.org/10.1039/C4CP04114C

[30] Vinod, K., Kumar, R.G.A. and Syamaprasad, U. (2007) Prospects for MgB_2 Superconductors for Magnet Application. *Superconductor Science and Technology*, **20**, R1-R13. https://doi.org/10.1088/0953-2048/20/1/R01

[31] D'Astuto, M., Heid, R., Renker, B., Weber, F., Schober, H., De la Pena-Seaman, O.,

Karpinski, J., Zhigadlo, N.D., Bossak, A. and Krisch, M. (2016) Non-Adiabatic Effects in the Phonon Dispersion of $Mg_{1-x}Al_xB_2$. *Physical Review B*, **93**, 1-5.

[32] Born, M. and Oppenheimer, R. (1927) Zur Quantentheorie der Molekeln. *Annalen der Physik*, **389**, 457-484. https://doi.org/10.1002/andp.19273892002

[33] Schutte, C.J.H. (1971) The Adiabatic Born-Oppenheimer Approximation. *Quarterly Reviews*, *Chemical Society*, **25**, 393-405. https://doi.org/10.1039/QR9712500393

[34] Boeri, L., Bachelet, G.B., Cappelluti, E. and Pietronero, L. (2002) Small Fermi Energy and Phonon Anharmonicity in MgB_2 and Related Compounds. *Physical Review B*, **65**, Article ID: 214501. https://doi.org/10.1103/PhysRevB.65.214501

[35] Uchiyama, H., Shen, K.M., Lee, S., Damascelli, A., Lu, D.H., Feng, D.L., Shen, Z.-X. and Tajima, S. (2002) Electronic Structure of MgB_2 from Angle-Resolved Photoemission Spectroscopy. *Physical Review Letters*, **88**, Article ID: 157002. https://doi.org/10.1103/PhysRevLett.88.157002

[36] Kang, W.N., Jung, C.U., Kim, K.H., Park, M.-S., Lee, S.Y., Kim, H.-J., Choi, E.-M., Kim, K.H., Kim, M.-S. and Lee, S.-I. (2001) Hole Carrier in MgB_2 Characterized by Hall Measurements. *Physical Review Letters*, **79**, 982-984. https://doi.org/10.1063/1.1392979

[37] Kang, W.N., Kim, H.-J., Choi, E.-M., Kim, H.J., Kim, K.H.P., Lee, H.S. and Lee, S.-I. (2002) Hall Effect in *c*-axis-oriented MgB_2 Thin Films. *Physical Review B*, **65**, Article ID: 134508. https://doi.org/10.1103/PhysRevB.65.134508

[38] Suzuki, S., Higai, S.I. and Nakao, K. (2001) Two-Dimensional σ-Hole Systems in Boron Layers: A First-Principles Study on $Mg_{1-x}Na_xB_2$ and $Mg_{1-x}Al_xB_2$. *Journal of the Physical Society of Japan*, **70**, 1206-1209. https://doi.org/10.1143/JPSJ.70.1206

[39] Ashcroft, N.W. and Mermin, N.D. (1976) Solid State Physics. Saunders, Philadelphia.

[40] Calandra, M., Lazzeri, M. and Mauri, F. (2007) Review: Anharmonic and Non-Adiabatic Effects in MgB_2: Implications for the Isotope Effect and Interpretation of Raman Spectra. *Physica C: Superconductivity*, **456**, 38-44. https://doi.org/10.1016/j.physc.2007.01.021

[41] Bardeen, J. (1951) Electro-Vibration Interactions and Superconductivity. *Reviews of Modern Physics*, **23**, 261-270. https://doi.org/10.1103/RevModPhys.23.261

[42] de la Penha, O., Aguayo, A. and de Coss, R. (2002) Effects of Al Doping on the Structural and Electronic Properties of $Mg_{1-x}Al_xB_2$. *Physical Review B*, **66**, Article ID: 012511.

[43] Bianconi, A. (2005) Feshbach Shape Resonance in Multiband Superconductivity in Heterostructures. *Journal of Superconductivity*, **18**, 626-636. https://doi.org/10.1007/s10948-005-0047-5

[44] Johannes, M.D. and Mazin, I.I. (2008) Fermi Surface Nesting and the Origin of Charge Density Waves in Metals. *Physical Review B*, **77**, Article ID: 165135. https://doi.org/10.1103/PhysRevB.77.165135

[45] Jorgensen, J.D., Hinks, D.G. and Short, S. (2001) Lattice Properties of MgB_2 versus Temperature and Pressure. *Physical Review B*, **63**, Article ID: 224522.

[46] Lortz, R., Wang, Y., Abe, S., Meingast, C., Paderno, Y.B., Filippov, V. and Junod, A. (2005) Specific Heat, Magnetic Susceptibility, Resistivity and Thermal Expansion of the Superconductor ZrB_{12}. *Physical Review B*, **72**, Article ID: 024547. https://doi.org/10.1103/PhysRevB.72.024547

[47] Anshukova, N.V., Bulychev, B.M., Golovashkin, A.I., Ivanova, L.I., Krynetskii, I.B., Minakov, A.A. and Rusakov, A.P. (2003) Anomalous Low-Temperature Behavior of

the Thermal Characteristics of MgB$_2$. *Journal of Experimental and Theoretical Physics*, **97**, 70-77. https://doi.org/10.1134/1.1600798

[48] Shi, L., Zhang, H., Chen, L. and Feng, Y. (2004) The Raman Spectrum and Lattice Parameters of MgB$_2$ as a Function of Temperature. *Journal of Physics: Condensed Matter*, **16**, 6541-6550. https://doi.org/10.1088/0953-8984/16/36/019

[49] Wu, S.Y., Shih, P.-H., Ji, J.-Y., Chan, T.-S. and Yang, C.C. (2016) Direct Observation of Charge Re-Distribution in a MgB$_2$ Superconductor. *Superconductor Science and Technology*, **29**, Article ID: 045001. https://doi.org/10.1088/0953-2048/29/4/045001